

See discussions, stats, and author profiles for this publication at: <https://www.researchgate.net/publication/26832372>

Real-Time Chemical Imaging of Bacterial Activity in Biofilms Using Open-Channel Microfluidics and Synchrotron FTIR Spectromicroscopy

ARTICLE *in* ANALYTICAL CHEMISTRY · SEPTEMBER 2009

Impact Factor: 5.64 · DOI: 10.1021/ac9015424 · Source: PubMed

CITATIONS

52

READS

73

6 AUTHORS, INCLUDING:



Hoi-ying Holman

Lawrence Berkeley National Laboratory

92 PUBLICATIONS 1,934 CITATIONS

SEE PROFILE



Zhao Hao

University of California, Berkeley

70 PUBLICATIONS 3,023 CITATIONS

SEE PROFILE

Real-Time Chemical Imaging of Bacterial Activity in Biofilms Using Open-Channel Microfluidics and Synchrotron FTIR Spectromicroscopy

Hoi-Ying N. Holman,^{*,†} Robin Miles,[‡] Zhao Hao,[†] Eleanor Wozei,[†] L. Meadow Anderson,[§] and Haw Yang[§]

Lawrence Berkeley National Laboratory, 1 Cyclotron Road, Berkeley, California 94720, Lawrence Livermore National Laboratory, 7000 East Avenue, Livermore, California 94550, and Chemistry Department, University of California, Berkeley, California 94720

Real-time chemical imaging of bacterial activities can facilitate a comprehensive understanding of the dynamics of biofilm structures and functions. Synchrotron-radiation-based Fourier transform infrared (SR-FTIR) spectromicroscopy can yield high spatial resolution and label-free vibrational signatures of chemical bonds in biomolecules, but the abundance of water in biofilms has hindered SR-FTIR's sensitivity in investigating bacterial activity. We developed a simple open-channel microfluidic system that can circumvent the water-absorption barrier for chemical imaging of the developmental dynamics of bacterial biofilms with a spatial resolution of several micrometers. This system maintains a 10 μm thick laminar-flow-through biofilm system that minimizes both the imaging volume in liquid and the signal interference from geometry-induced fringing. Here we demonstrate the ability of the open-channel microfluidic platform to maintain the functionality of living cells while enabling high-quality SR-FTIR measurements. We include several applications that show how microbes in biofilms adapt to their immediate environments. The ability to directly monitor and map bacterial changes in biofilms can yield significant insight into a wide range of microbial systems, especially when coupled to more sophisticated microfluidic platforms.

Bacterial biofilms are structured dynamic communities of aggregated cells enclosed in a self-produced polymeric matrix that adheres to both inert and living surfaces in aqueous environments.^{1–3} These sessile communities are usually highly heterogeneous and exhibit complex biochemical processes such as metabolic cascades and cell–cell communications that differ significantly from cells in a planktonic state.^{4–6} For example, when opportunistic

pathogenic bacteria develop biofilms, they can become up to 1000 times more resistant to antibiotics.⁷ The formation of biofilms and their resistance to antibiotics and host immune attacks are at the root of many persistent and chronic bacterial infections.^{2,8,9} Real-time monitoring of bacterial activity at a chemical level during biofilm initiation, growth, release and bacteria–drug interactions in real time as the processes are happening could lead to new preventive and curative treatments.

Methods such as fluorescence microscopy,⁷ nuclear magnetic resonance (NMR) microscopy,¹⁰ and Raman microscopy^{11–13} have been used toward this end. However, these techniques have their own constraints when applied to the studies of living bacterial cells. In fluorescence microscopy, bacterial cells are required to have either an addition of fluorescent labels or the use of genetically engineered strains that produce fluorescent reporter proteins; both strategies may affect bacterial physiology.⁷ Furthermore, fluorescent labels have also been used as probes to predict the spatial distribution of drug uptake by cells when forming biofilms,^{7,14} but the sizes of fluorescent labels are generally larger than the drug molecules and may alter the drug transport properties and biological activity. Similarly, NMR requires labeled substrates (for example, ¹³C-labeled lactate), which may affect bacterial physiology. In contrast, Raman microscopy is label-free, but the low signal yields relative to the incident power are a challenge for the biofilm applications. Published applications of Raman microscopy to investigating live biofilm chemistry have been limited to the utilization of lasers typically with mean powers of >20 mW.^{12,13} However,

(5) Davies, D. G.; Parsek, M. R.; Pearson, J. P.; Igleswski, B. H.; Costerton, J. W.; Greenberg, E. P. *Science* **1998**, *280*, 295–298.

(6) De Kievit, T. R.; Gillis, R.; Marx, S.; Brown, C.; Igleswski, B. H. *Appl. Environ. Microb.* **2001**, *67*, 1865–1873.

(7) Stewart, P. S.; Franklin, M. J. *Nat. Rev. Microbiol.* **2008**, *6*, 199–210 (and the references cited therein).

(8) Drenkard, E.; Ausubel, F. M. *Nature* **2002**, *416*, 740–743.

(9) O'Toole, G. A.; Stewart, P. S. *Nat. Biotechnol.* **2005**, *23*, 1378–1379.

(10) Majors, P. D.; McLean, J. S.; Pinchuk, G. E.; Fredrickson, J. K.; Gorby, Y. A.; Minard, K. R.; Wind, R. A. *J. Microbiol. Meth.* **2005**, *62*, 337–344.

(11) Suci, P. A.; Geesey, G. G.; Tyler, B. J. *J. Microbiol. Methods* **2001**, *46*, 193–208.

(12) Ivleva, N. P.; Wagner, M.; Horn, H.; Niessner, R.; Haisch, C. *Anal. Bioanal. Chem.* **2009**, *393*, 197–206.

(13) Wagner, M.; Ivleva, N. P.; Haisch, C.; Niessner, R.; Horn, H. *Water Res.* **2009**, *43*, 63–76.

(14) Stephens, D. J.; Allan, V. J. *Science* **2003**, *300*, 82–86.

* To whom correspondence should be addressed. Phone: (510) 486-5943. Fax: (510) 486-7152. E-mail: hyholman@lbl.gov.

[†] Lawrence Berkeley National Laboratory.

[‡] Lawrence Livermore National Laboratory.

[§] University of California, Berkeley.

(1) Moller, S.; Pedersen, A. R.; Poulsen, L. K.; Arvin, E.; Molin, S. *Appl. Environ. Microbiol.* **1996**, *62*, 4632–4640.

(2) Costerton, J. W.; Stewart, P. S.; Greenberg, E. P. *Science* **1999**, *284*, 1318–1322.

(3) Whitchurch, C. B.; Tolker-Nielsen, T.; Ragas, P. C.; Mattick, J. S. *Science* **2002**, *295*, 1487–1487.

(4) Shapiro, J. A. *Annu. Rev. Microbiol.* **1998**, *52*, 81–104.

multiphoton fluorescence microscopy studies^{15–17} and Raman confocal microscopy study¹⁸ designed to identify effects of using visible and near-infrared lasers on cells reveal that mean laser powers in the range of watts to tens of milliwatts can affect cellular activity because it often generates heat or photoproducts.

Synchrotron-radiation-based Fourier transform infrared (SR-FTIR) spectromicroscopy has been used as a label-free approach to track biogeochemical changes with high sensitivity and micrometer spatial resolution in real time.¹⁹ Recently, we demonstrated that SR-FTIR is well-suited for monitoring chemical changes in bacteria during their stress-adaptive-response²⁰ since the mean power of a synchrotron mid-infrared beam is ~1 mW at the focused sample position, which is below the threshold for cytotoxic effects.²¹ However, applying SR-FTIR to study living bacteria activity in biofilms presented a major challenge because of the strong water absorption in the mid-infrared region. One approach used to suppress water absorption is attenuated total reflectance (ATR) for FTIR spectroscopy, but its $\leq 1\ \mu\text{m}$ penetration depth of the evanescent field captures information only from molecules at or near the interface.^{22,23} Another approach is to use a closed-channel microfluidic or an enclosed cuvette or flow cell with thin spacers to reduce the thickness of the aqueous layer to $<15\ \mu\text{m}$.^{24,25} However, our exploratory SR-FTIR experiments of biofilms in a closed-channel microfluidic device often revealed significant interference fringes in the spectrum. Interference between radiation that has been transmitted directly through the substrate or sample with light that has been reflected internally can cause spectrum fringes.²⁶ Because the spacing of these sinusoidal patterns typically varied, the fringes were not readily removed and spectral interpretation became difficult.

Here we evaluate the potential of an open-channel microfluidic approach to minimize water-absorption and the interference fringe problem while maintaining the functionality of microbial cells and capturing molecular information about microbial processes within biofilms over time. Taking advantage of this open-channel microfluidic SR-FTIR platform as a label-free approach for real-time imaging of bacterial activity in biofilms, we showed data differentiating *Escherichia coli* (*E. coli*) responses in biofilms to the DNA-targeted antibiotic mitomycin-C (MMC). MMC is a biore-

ductive chemical that is very stable ex vivo and is activated only after it has entered the cells.²⁷ We also showed data of effects of geometry on the synthesis of glycocalyx (a bacterial carbohydrate²⁸ that facilitates strong adhesion of bacteria to surfaces and between cells) and other key biomolecules during biofilm development in microscopic space. Our results show that by combining our open-channel system with SR-FTIR spectromicroscopy, we are able to maintain a living bacteria community on biofilm over a long period of time while making continuous spectroscopic measurements and chemical imaging.

MATERIALS AND METHODS

Chemicals and Bacteria. Glucose and antibiotics kanamycin and mitomycin-C (MMC) were purchased from Sigma-Aldrich. Luria–Bertani (LB) broth and granulated agar were purchased from Fisher Scientific. The recombinant bioluminescent strain *Escherichia coli* DPD2794²⁹ was a gift from Dr. LaRossa (DuPont Experimental Station, Wilmington, DE), which were stored at $-80\ ^\circ\text{C}$ until use. The bacterial plasmid pRecALux3 contains a transcriptional fusion of the DNA damage-inducible promoter *recA* to the *Vibrio fischeri luxCDABE* operon, which confers resistance to kanamycin and ampicillin²⁹ but not to our model antibiotic MMC. The bioluminescence MMC sublethal toxicity assay reveals for planktonic *E. coli* a significant cell impairment/death when the MMC concentration is above $0.125\ \mu\text{g/mL}$ (Supporting Information, Figure S-3). In our biofilm study, we used a concentration of $0.15\ \mu\text{g/mL}$.

Microfluidic Design and Experimental Setup. One main challenge in our approach was to create a continuous thin-film ($<15\ \mu\text{m}$) laminar flow despite evaporation in an open microchannel while creating a controlled aqueous environment that supplies sufficient nutrients and removes metabolic wastes for prolonged experimental observations. To meet the challenge, we fabricated a simple open-channel microfluidic device using a 1 cm diameter silicon chip upon which hydrophilic microstructures were formed by deep reactive ion etching (Figure 1b). In this study, the deep reactive ion etched microchannels on the silicon chip were $20\text{--}40\ \mu\text{m}$ wide and 1 mm long, whereas the square microwells were about $50\ \mu\text{m}$ wide, and both were $10\text{--}15\ \mu\text{m}$ deep. The silicon surface was then functionalized (see Supporting Information).

A continuous open-microchannel flow was maintained by a balance between the hydrostatic pressure at the inlet and the capillary pulls at the outlet (Figure 1a). Specifically, a nonpulsating continuous open-channel flow was maintained by hydrostatic pressure in a microliter-size feeder droplet at the microchannel inlet that was supplied from an off-chip reservoir. A wicking mechanism at the outlet provided the additional capillary forces needed to continuously “pull” the thin liquid film. A flow map (Figure 1c) for the microfluidic device used in this study was obtained by a fluid dynamic simulation based on the experimental parameters measured on a flow with polystyrene beads inside the microstructures (see Supporting Information). The bulk flow rate in the open microchannel was set to $\sim 60\ \mu\text{m/s}$. As biofilms formed and grew in the microstructures, higher pressure gradients were

- (15) Hockberger, P. E.; Skimina, T. A.; Centonze, V. E.; Lavin, C.; Chu, S.; Dadras, S.; Reddy, J. K.; White, J. G. *Proc. Natl. Acad. Sci. U.S.A.* **1999**, *96*, 6255–6260.
- (16) König, K.; Becker, T. W.; Fischer, P.; Riemann, I.; Halbhauer, K. J. *Opt. Lett.* **1999**, *24*, 113–115.
- (17) Squirrell, J. M.; Wokosin, D. L.; White, J. G.; Bavister, B. D. *Nat. Biotechnol.* **1999**, *17*, 763–767.
- (18) Kang, L. L.; Huang, Y. X.; Luo, M. *Spectrosc. Spectral Anal.* **2008**, *28*, 2343–2347.
- (19) Holman, H.-Y. N.; Martin, M. C. In *Advances in Agronomy*; Sparks, D., Ed.; Elsevier: New York, 2006; Vol. 90, pp 79–127.
- (20) Holman, H.-Y. N.; Wozel, E.; Lin, Z.; Comolli, L. R.; Ball, D. A.; Borglin, S.; Fields, M. W.; Hazen, T. C.; Downing, K. H. *Proc. Natl. Acad. Sci. U.S.A.* **2009**, *106*, 12599–12604.
- (21) Holman, H.-Y. N.; Bjornstad, K. A.; McNamara, M. P.; Martin, M. C.; McKinney, W. R.; Blakely, E. A. *J. Biomed. Opt.* **2002**, *7*, 417–424.
- (22) Nivens, D. E.; Chambers, J. Q.; Anderson, T. R.; Tunlid, A.; Smit, J.; White, D. C. *J. Microbiol. Methods* **1993**, *17*, 199–213.
- (23) Jiang, W.; Saxena, A.; Song, B.; Ward, B. B.; Beveridge, T. J.; Myneni, S. C. *Langmuir* **2004**, *20*, 11433–11442.
- (24) Moss, D. A.; Keese, M.; Pepperkok, R. *Vib. Spectrosc.* **2005**, *38*, 185–191.
- (25) Kaun, N.; Kulka, S.; Frank, J.; Schade, U.; Vellekoop, M. J.; Harasek, M.; Lendl, B. *Analyst* **2006**, *131*, 489–494.
- (26) Griffiths, P. R.; de Haseth, J. A. *Fourier Transform Infrared Spectrometry*, 2nd ed.; Wiley-Interscience: Hoboken, NJ, 2007.

(27) Tomasz, M.; Palom, Y. *Pharmacol. Ther.* **1997**, *76*, 73–87.

(28) Costerton, J. W.; Cheng, K. J.; Geesey, G. G.; Ladd, T. I.; Nickel, J. C.; Dasgupta, M.; Marrie, T. J. *Annu. Rev. Microbiol.* **1987**, *41*, 435–464.

(29) Vollmer, A. C.; Belkin, S.; Smulski, D. R.; Vandyk, T. K.; Larossa, R. A. *Appl. Environ. Microbiol.* **1997**, *63*, 2566–2571.

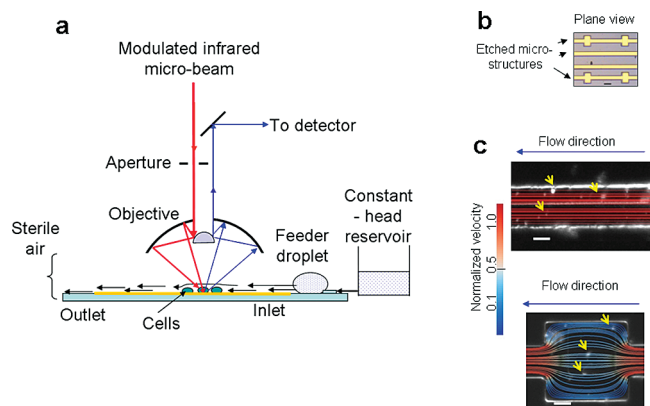


Figure 1. (a) Microfluidic SR-FTIR microscopy platform design and setup. (b) Plane view depicts an example chip with several parallel etched microstructures for multiple simultaneous experiments. (c) Flow maps of the microstructures, simulated from experimentally measured path-lines of near-neutral density polystyrene beads (yellow arrows), are superimposed on a snapshot image of the flow visualization experiment (Reynold's number between 0.05 and 0.6): top, flow in a microchannel; bottom, flow in a microwell. All applications depicted in Figures 2–4 were conducted with the maximum flow velocity set at $\sim 60 \mu\text{m/s}$. Scale bars = $40 \mu\text{m}$.

required to maintain the flow, which was achieved by finely adjusting the elevation of the off-chip reservoir. We had confirmed in our validation study that by continuously maintaining the thin-film laminar flow in the experimental platform, our open-channel SR-FTIR approach yields high-quality stable infrared measurements with minimal water inference while providing adequate sustenance for living bacteria (see Supporting Information, Figures S-1 and S2).

Bacterial Seeding and Biofilm Initiation. Prior to each experiment, an overnight *E. coli* DPD2794 batch culture was grown by inoculating a single colony of the strain (grown from the frozen stock on a LB agar plate) into 10 mL of fresh LB medium containing $50 \mu\text{g/mL}$ kanamycin and incubated at room temperature ($\sim 26^\circ\text{C}$). The overnight culture was diluted 1:10 in fresh, modified LB medium containing 0.25 g/L glucose and $50 \mu\text{g/mL}$ kanamycin. The culture was grown to log phase (as measured by $\text{OD}_{600\text{nm}} = 0.2$), and $1 \mu\text{L}$ of the cell suspension was inoculated into the microfluidic device. Prior to inoculation the influent line from the LB medium reservoir was clamped to prevent back-growth during the inoculation. After 2 h, the medium flow was started at a high flow rate to “flush out” unattached cells before lowering the flow velocity to $\sim 60 \mu\text{m/s}$ and allowing biofilm initiation and growth.

Mitomycin-Biofilm Experiment. A similar bacterial seeding and biofilm initiation procedure was used to culture biofilms in microchannels. At 24 h after the formation of a biofilm, the flow system was switched to using LB medium containing $0.15 \mu\text{g/mL}$ of mitomycin-C.

SR-FTIR Measurement. All SR-FTIR measurements were made on the microfluidic device in conjunction with a Nicolet Magna 760 FTIR bench and a Nicolet Nic-Plan IR microscope (Thermo Scientific Inc., Waltham, MA) at the infrared beamline 1.4.3 of the Advanced Light Source (Lawrence Berkeley National Laboratory, Berkeley, CA; <http://infrared.als.lbl.gov/>). Mid-infrared photons emitted from the synchrotron were focused by

the all-reflective optics infrared microscope (Figure 1a) with a numerical aperture (NA) objective ($\text{NA} = 0.65$) through bacteria onto the gold-coated surface inside the microfluidic device. SR-FTIR measurements over a mid-infrared wavenumber range of $650\text{--}4000 \text{ cm}^{-1}$ were made by the transfection mode over time using Thermo Electron's Omnic 7.2 (<http://www.thermo.com/>). Each real-time spectrum represents an average of 64 scans at a spectral resolution of 4 cm^{-1} with an absorption peak position accuracy of $1/100 \text{ cm}^{-1}$. To image the biochemical properties and the distribution of bacterial activity, we typically divided the entire view field of the biofilm into equal-sized $5 \mu\text{m} \times 5 \mu\text{m}$ squares before raster scanning, collecting full SR-FTIR spectra at each position. Because the current of the synchrotron decreased with time between electron refills during these studies, which occurred every 9 h, the beam intensity decreased proportionally. A method of global baseline removal took this into account. A scaled SR-FTIR spectrum of water vapor was then subtracted immediately from each SR-FTIR spectrum to correct spectral contributions of water vapor. These “raw” SR-FTIR spectra were subjected to data preprocessing.

Data Preprocessing Considerations and Preprocessing.

Figure S-4 (Supporting Information) is an example of a series of real-time SR-FTIR measurements typical of bacterial attachment and early growth in the microfluidic device before preprocessing. They show well-resolved vibrational bands from carbohydrates and other key macromolecules superimposed on a broad baseline feature due to different background scatterings, biofilm thickness effects, and continuum water absorption.

We employed three different data preprocessing methods to remove these artifacts. For time-series analyses, we exported the “raw” SR-FTIR spectra to our in-house software package, which used the method of Kramers–Kronig (KK) constrained variational fitting³⁰ to fit the measured SR-FTIR spectra to identify individual peaks and baseline features. There are at least three mathematical models to remove baseline artifacts.^{30–33} We selected the KK-based multioscillator model because it inherits the robustness of the least-squares fitting and the ability of the KK analysis to extract the full spectral information.³⁰ This hybrid KK method provides a general applicability to all linear-response optical measurements as well as to combinations of reflectivity and scattering and absorption measurements made on different sample substrates without the need of readaptation. Figure S-5 (Supporting Information) demonstrates the typical fit of the KK simulation to the measurement SR-FTIR data. The peak strengths (after the baseline removal) were used in the time-series analysis. Preprocessing of the raw SR-FTIR spectra for chemical content analyses involved vector normalization and offset correction. This is to avoid interference from biomass of different thickness as well as baseline artifacts. Preprocessing of the raw SR-FTIR maps involved subtracting a linear baseline from four spectrum segments with end points at minima near 890, 950, 1005, 1180, 1370, and 1480 cm^{-1} . These baseline points were consistent with results from

- (30) Kuzmenko, A. B. *Rev. Sci. Instrum.* **2005**, *76*, 1–10.
- (31) Gallagher, N. B.; Blake, T. A.; Gassman, P. L. *J. Chemom.* **2005**, *19*, 271–281.
- (32) Helland, I. S.; Naes, T.; Isaksson, T. *Chemom. Intell. Lab. Syst.* **1995**, *29*, 233–241.
- (33) Romeo, M.; Mohlenhoff, B.; Diem, M. *Vib. Spectrosc.* **2006**, *42*, 9–14.

the KK simulation of experimental spectra selected from the spectral data pool.

Spectral Markers for Chemical Imaging. The spectral analysis for synchrotron and for conventional infrared spectra is identical, in accordance to the first principle of vibrational spectroscopy, as shown in a number of synchrotron-based studies.^{18,26,27} Here the marker peaks selected for our biofilm dynamics study were the absorption peaks at $\sim 1080\text{ cm}^{-1}$ (dominated by the vibration of $\nu\text{C}-\text{O}-\text{C}$ and $\nu\text{C}-\text{O}-\text{P}$ in polysaccharides and of $\nu_{\text{as}}\text{PO}_2^-$ groups in nucleic acids), $\sim 1130\text{ cm}^{-1}$ (characteristic of stretching vibration mode of carbohydrate glycocalyx ($\nu\text{C}-\text{O}$)³⁴), $\sim 1240\text{ cm}^{-1}$ (mostly from the $\nu_{\text{as}}\text{PO}_2^-$ groups of DNA/RNA polysaccharides backbone structures), and $\sim 1310\text{ cm}^{-1}$ (characteristic of protein amide III with an in-phase combination of $\delta^{\text{ip}}\text{N}-\text{H}$ and $\nu_{\text{s}}\text{C}-\text{C}$, $\nu_{\text{s}}\text{C}-\text{N}$, and $\delta^{\text{ip}}\text{C}=\text{O}$). Figure S-6 (Supporting Information) is a snapshot of a series of real-time raw SR-FTIR spectra of *E. coli*-MMC interactions in the ring-vibration region ($900\text{--}1200\text{ cm}^{-1}$). MMC, an antibiotic that is activated only after it has entered a cell,^{35,36} is reduced to a hydroquinone form that covalently cross-links to guanine residues of DNA to form DNA-MMC adducts.³⁶ Time series analysis enabled us to establish that DNA-MMC adducts exhibit an infrared absorption band at $\sim 986\text{ cm}^{-1}$. We attributed this $\sim 986\text{ cm}^{-1}$ mode to the vibration from the deoxyribose-phosphate backbone of the DNA-MMC adduct. This absorption feature guided the imaging analysis of the *E. coli*-MMC interactions in the biofilm.

RESULTS AND DISCUSSION

To determine how well the microfluidic SR-FTIR spectromicroscopy approach performed, we first mapped the uptake of mitomycin-C by *Escherichia coli* within a biofilm (Figure 2a) in real time. Results are shown in Figure 2b. After being exposed to MMC for 8 h, SR-FTIR chemical maps show a much stronger DNA-MMC adduct signal ($\sim 986\text{ cm}^{-1}$; Figure 2b, lower left panel versus upper left panel), especially in areas that were either closer to the MMC source (locations no. 1 and no. 2) or in areas formerly rich in protein amide III (intensities at $\sim 1310\text{ cm}^{-1}$; Figure 2b, locations no. 3 and no. 4 in the upper middle panels). The SR-FTIR maps also show a close correlation between increased polysaccharides ($\sim 1080\text{ cm}^{-1}$; Figure 2b, lower right versus upper right panels, around locations no. 2 and no. 3) and decreased protein amide III signal ($\sim 1310\text{ cm}^{-1}$; Figure 2b, lower middle versus upper middle panels, around locations no. 2 and no. 3) in areas ahead of the “downstream” edge of the DNA-MMC adduct ($\sim 986\text{ cm}^{-1}$) concentrations (Figure 2b, lower left panel). In areas with little DNA-MMC adducts (Figure 2b, lower left panel, around location no. 6), the protein amide III signal ($\sim 1310\text{ cm}^{-1}$) increased with MMC exposure (Figure 2b, lower left versus lower middle panels, also around location no. 6). Our bright field microscopy observation shows that the bulk water crossed the sample field, yet the SR-FTIR image plot shows highly localized MMC uptake (Figure 2b, lower left panel). Previous studies of flow in biofilms show a much slower interstitial flow in biofilms

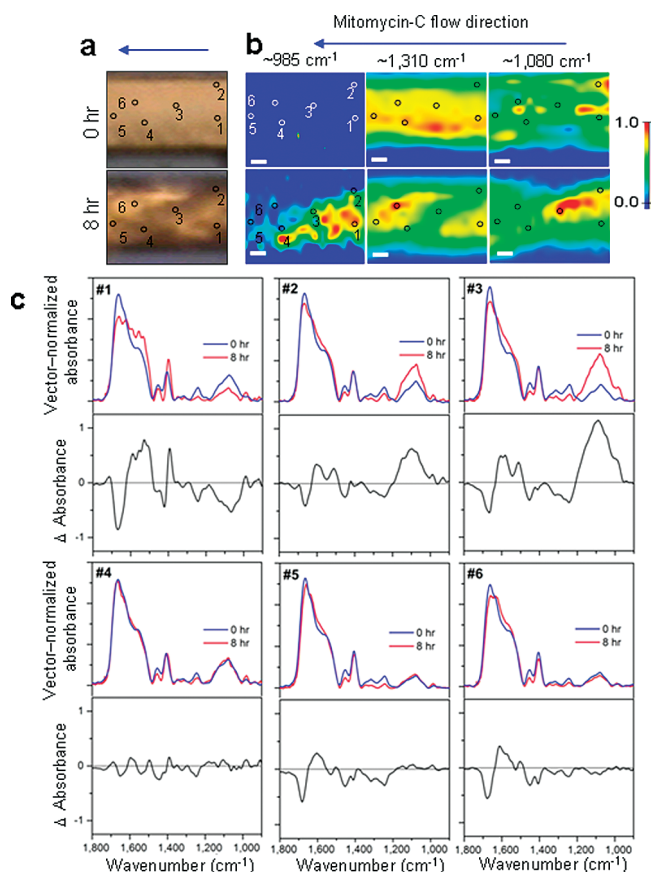


Figure 2. Spatial and temporal distributions of mitomycin-C uptake within a 1 day old *E. coli* biofilm. (a) Bright-field micrographs of the *E. coli* biofilm before ($t = 0$) and during ($t = 8\text{ h}$) mitomycin-C exposure. (MMC concentration, $0.15\text{ }\mu\text{g/mL}$). (b) 2-D SR-FTIR chemical image plots of the intensity, before (upper panels) and during (lower panels) MMC exposure, at $\sim 986\text{ cm}^{-1}$ (DNA-MMC adducts), $\sim 1310\text{ cm}^{-1}$ (protein amide III), and $\sim 1080\text{ cm}^{-1}$ (polysaccharides). Each panel pair was normalized to each maximum intensity separately. Notice the three distinct biochemical regions formed during MMC treatment: a high MMC-uptake and a low MMC-uptake region separated by an area of high polysaccharide content. Arrows indicate MMC stream direction. \circ in panels mark selected locations. Scale bars = $10\text{ }\mu\text{m}$. (c) Preprocessed SR-FTIR spectra at selected locations before (blue spectra) and during (red spectra) MMC exposure. They were vector-normalized over the $900\text{--}1780\text{ cm}^{-1}$ region and offset corrected. (See “raw” spectra in Figure S-7, Supporting Information, for comparison). The difference spectra (black spectra) below were obtained by 1-to-1 subtraction of vector-normalized spectra. Notice the significant loss of signals in the low-frequency region ($900\text{--}1400\text{ cm}^{-1}$) at location no. 1 and an elevated production of polysaccharides content ($\sim 1080\text{ cm}^{-1}$) at locations no. 2 and no. 3. Arrows indicate medium flow direction.

or even a flow regime dominated by diffusion.³⁷ We speculated that the localization of MMC indicates some possible internal flow diversions around the parts of higher protein amide III signal and that the transport of mitomycin-C through these regions seems greatly retarded probably as a result of flow heterogeneity inside the biofilms.

Spectromicroscopy analyses at different locations (Figure 2a,b, black circles) disclose localized changes in biochemical contents caused by MMC exposure (compare the spectra at each location

(34) Zeroual, W.; Choisy, C.; Doglia, S. M.; Bobichon, H.; Angiboust, J. F.; Manfait, M. *Biochim. Biophys. Acta (Mol. Cell Res.)* **1994**, *1222*, 171–178.

(35) Iyer, V. N.; Szybalski, W. *Science* **1964**, *145*, 55–58.

(36) Portugal, J.; Sanchezbaeza, F. J. *Biochem. J.* **1995**, *306*, 185–190.

(37) Debeer, D.; Stoodley, P.; Lewandowski, Z. *Biotechnol. Bioeng.* **1994**, *44*, 636–641.

recorded at $t = 0$ versus $t = 8$ h). An easy way to analyze and understand the key biochemical changes is to compare the vector-normalized spectra (over the 900–1800 cm^{-1} region) at the two time points, as shown in Figure 2c with difference spectra below. The difference spectra were obtained by a one-to-one subtraction of the vector-normalized spectra. In Figure 2c, location no. 1 (in the DNA-MMC concentration area in Figure 2b, lower left panel) exhibits a significant decrease in infrared intensity in the low-frequency fingerprint region ($\sim 1000\text{--}1400\text{ cm}^{-1}$), suggesting a loss of intracellular contents as is typical of lysed bacterial cells. At the same time, it also shows a significant increase in the absorption intensity between 1600 and 1500 cm^{-1} , with a shoulder at ~ 1510 and other spectral fine structures within the region. These frequencies are in the spectral region of the DNA alkylation species of DNA-MMC adducts.^{38–40} The absorption features at ~ 1510 and $\sim 1600\text{ cm}^{-1}$ correspond to a monofunctional binding of MMC to DNA that forms a monoadduct MMC-d(GpC).⁴⁰ The additional absorption features within the 1500–1600 cm^{-1} region are contributions from a covalent cross-link MMC-DNA bisadduct.³⁹ Locations no. 2 and no. 3, which are in the areas along and ahead of the downstream edge of the DNA-MMC adduct concentrations, exhibit increasing contents of polysaccharides ($\sim 1080\text{ cm}^{-1}$) and a moderate-to-minor uptake of MMC and an accumulation of the predominantly DNA-MMC monoadduct. Location no. 4 contrastingly exhibits stable chemical compositions, and very little DNA-MMC adduct formation. Its neighboring locations no. 5 and no. 6, however, show a moderate formation of mixed DNA-MMC adducts. These heterogeneous spectral features and behavior at locations no. 2 to no. 6 may reflect cellular diversification processes in response to MMC toxicity. Bacteria diversified in biofilms that resist heavy metal toxicities;⁴¹ diversification processes may include metabolic modification and/or migration to more favorable living areas.⁴²

We next illustrate the microfluidic SR-FTIR technique by turning to a less explored yet critical aspect of biofilm formation and release. Many microbial processes important in pathogenesis and ecology are initiated in confined microscopic spaces.^{43–46} Recent reports indicate that colonizing bacterial cells actively seek out confined spaces⁴⁶ where biofilm initiation and formation could be influenced by nutrient supplies and waste removal. Here we used our microfluidic SR-FTIR microscopy platform to compare

the dynamics of biofilm formation in microchannels (higher nutrient supplies/mass exchange; see the upper panel of Figure 1c) with microwells (lower nutrient supplies/waste removal; see the lower panel of Figure 1c). We first monitored the SR-FTIR signal at a fixed location over a 9 h period and then used the raster mapping mode to obtain SR-FTIR chemical images of biofilms in each microstructure by collecting full SR-FTIR spectra at each position. Results for the microchannel and the microwell biofilms are shown in Figures 3 and 4.

Time-course analysis of the SR-FTIR measurements made in a microchannel shows a sequence of biomolecule synthesis events during biofilm development (Figure 3a). After a 30 min lag (Figure 3a and insert, blue dots), the polysaccharide intensity ($\sim 1080\text{ cm}^{-1}$) first rose exponentially for 30 min, then approached an asymptotic regime. The glycocalyx intensity at $\sim 1130\text{ cm}^{-1}$ (between ~ 1145 and 1120 cm^{-1}) is similar, but with an initial lag of approximately 40 min (Figure 3a and insert, black squares). The vibration intensities of the phosphodiester (PO_2^-) groups of DNA/RNA polysaccharide backbone structures ($\sim 1240\text{ cm}^{-1}$) and of the protein amide III ($\sim 1310\text{ cm}^{-1}$) began to increase after a longer lag of ~ 50 min, followed by only an additional 10 min of exponential production that gave way to a slower growth regime (Figure 3a, magenta circles and green triangles). To image the distribution of these four bacterial components in a larger region ($85\text{ }\mu\text{m} \times 40\text{ }\mu\text{m}$) of the biofilm (Figure 3c, insert), we divided the entire region into equal-sized $5\text{ }\mu\text{m} \times 5\text{ }\mu\text{m}$ squares before raster scanning, collecting full SR-FTIR spectra at each position. The image plots of marker bands (Figure 3c) reveal abundant glycocalyx carbohydrates (at $\sim 1130\text{ cm}^{-1}$) for strong adhesion, its close spatial association with other polysaccharide carbohydrates (at $\sim 1080\text{ cm}^{-1}$), and protein amide III ($\sim 1310\text{ cm}^{-1}$) signals, possibly characteristic of stable *E. coli* biofilms. This provides direct evidence that glycocalyx synthesis is prerequisite to the formation of bacterial biofilms.⁴⁷

Unlike the microchannel data, where the signal intensity of key biomolecules appeared to approach an asymptotic state (Figure 3a), the microwell SR-FTIR absorbance exhibited cyclicity (Figure 4a), a sequential rise and fall of different biomolecule signal intensities—the amide III ($\sim 1310\text{ cm}^{-1}$) intensities plateau, only to collapse once polysaccharide and nucleic acid bands (~ 1080 and $\sim 1240\text{ cm}^{-1}$) have dropped to nearly their initial values. Light microscopy observations in parallel experiments detected bacteria or debris moving downstream periodically. Losing the biofilm materials may have preceded the escape of *E. coli* from the matrix between growth periods, but this has not yet been demonstrated directly. It is unlikely that biofilm materials were consumed by *E. coli* cells before their escape. The unlikely bacterial utilization of intercellular polysaccharides during biofilm decay under conditions of nutrient limitation has been discussed by another group.⁴⁸

The chemical image plots obtained after the second release show locally higher signal intensities of protein amide III ($\sim 1310\text{ cm}^{-1}$; Figure 4b, lower left panel) and DNA/RNA polysaccharides

(38) Tomasz, M.; Chowdary, D.; Lipman, R.; Shimotakahara, S.; Veiro, D.; Walker, V.; Verdine, G. L. *Proc Natl. Acad. Sci. U.S.A.* **1986**, *83*, 6702–6706.

(39) Tomasz, M.; Lipman, R.; Chowdary, D.; Pawlak, J.; Verdine, G. L.; Nakanishi, K. *Science* **1987**, *235*, 1204–1208.

(40) Tomasz, M.; Lipman, R.; Snyder, J. K.; Nakanishi, K. *J. Am. Chem. Soc.* **1983**, *105*, 2059–2063.

(41) Harrison, J. J.; Ceri, H.; Turner, R. J. *Nat. Rev. Microbiol.* **2007**, *5*, 928–938.

(42) Thoma, C.; Frank, M.; Rachel, R.; Schmid, S.; Nather, D.; Wanner, G.; Wirth, R. *Environ. Microbiol.* **2008**, *10*, 2785–2795.

(43) Park, S.; Wolanin, P. M.; Yuzbashyan, E. A.; Lin, H.; Darnton, N. C.; Stock, J. B.; Silberzan, P.; Austin, R. *Proc. Natl. Acad. Sci. U.S.A.* **2003**, *100*, 13910–13915.

(44) Park, S.; Wolanin, P. M.; Yuzbashyan, E. A.; Silberzan, P.; Stock, J. B.; Austin, R. H. *Science* **2003**, *301*, 188–188.

(45) Jonsson, H.; Levchenko, A. *Multiscale Model Sim.* **2005**, *3*, 346–361.

(46) Cho, H. J.; Jonsson, H.; Campbell, K.; Melke, P.; Williams, J. W.; Jedynak, B.; Stevens, A. M.; Groisman, A.; Levchenko, A. *PLoS Biol.* **2007**, *5*, 2614–2623.

(47) Costerton, J. W.; Irvin, R. T.; Cheng, K. J. *Annu. Rev. Microbiol.* **1981**, *35*, 299–324.

(48) Jager, S.; Mack, D.; Rohde, H.; Horstkotte, M. A.; Knobloch, J. K. M. *Appl. Environ. Microbiol.* **2005**, *71*, 5577–5581.

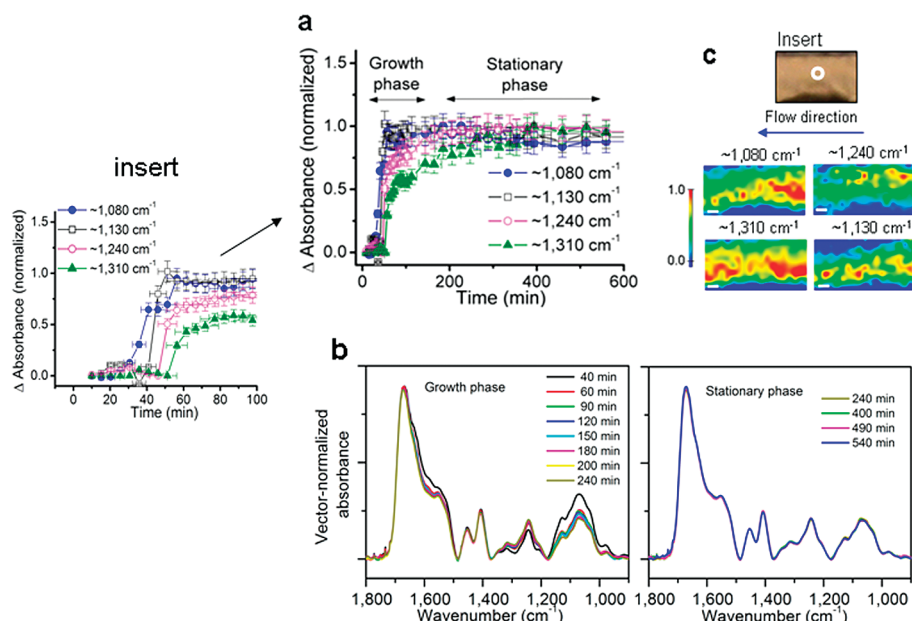


Figure 3. Biofilm dynamics in a microchannel (see flow field in Figure 1c, upper panel). (a) Transient biochemistry during biofilm development as shown by the normalized intensity of the four molecular markers at $\sim 1,080\text{ cm}^{-1}$ (polysaccharides), $\sim 1,130\text{ cm}^{-1}$ (glycocalyx), $\sim 1,240\text{ cm}^{-1}$ (DNA/RNA polysaccharides), and $\sim 1,310\text{ cm}^{-1}$ (protein amide III). (b) Snapshots of preprocessed SR-FTIR spectra of *E. coli* biofilm in a microchannel for selected time points. They were vector-normalized over the $900\text{--}1780\text{ cm}^{-1}$ region and offset corrected. (c) 2-D SR-FTIR images of each of these four molecular marker bands within the *E. coli* biofilm in the microchannel. Each panel pair was normalized to their maximum intensity. Insert, bright field micrographs. \circ in the insert marks the location of the transient biochemistry analysis. Arrows indicate medium flow direction. Scale bars = $10\text{ }\mu\text{m}$.

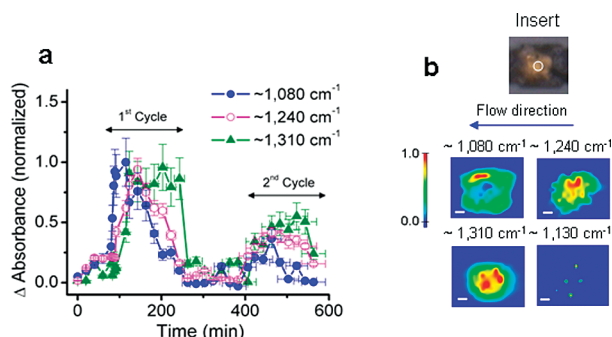


Figure 4. Biofilm dynamics in a microwell (see flow field in Figure 1c, lower panel). (a) Transient biochemistry during biofilm development as shown by the normalized intensity of the three molecular markers at $\sim 1,080\text{ cm}^{-1}$ (polysaccharides), $\sim 1,240\text{ cm}^{-1}$ (DNA/RNA polysaccharides), and $\sim 1,310\text{ cm}^{-1}$ (protein amide III). Intensity at $\sim 1,130\text{ cm}^{-1}$ (carbohydrate glycocalyx) is weak and thus not shown. (b) 2-D SR-FTIR chemical images of the *E. coli* biofilms in the microwell. Each panel pair was normalized to the maximum intensity. Insert, bright field micrograph. \circ in the insert marks the location of the transient biochemistry analysis. Arrows indicate flow direction. Scale bars = $10\text{ }\mu\text{m}$.

(at $\sim 1,240\text{ cm}^{-1}$) near the microwell center (Figure 4b, upper right panel), whereas the polysaccharide matrix accumulated near the microwell edge (Figure 4b, upper left panel). There is little spectroscopic evidence of glycocalyx ($\sim 1,130\text{ cm}^{-1}$; Figure 4b, lower right panel) to facilitate strong adherence to the microwell substrate. The lack of glycocalyx and the minimal spatial association between key biofilm molecules suggest that either the biofilms became unstable prior to release or the cells in the microwell were in a loosely attached state. From our data, we initially believed that the lower convective transport (i.e., lower nutrient supplies/waste removal) in the microwell geometry

affected the bacterial biofilm formation. However, similar results were observed when the flow velocity inside the microwell doubled. In our experimental conditions, cells did not grow monotonically to very high density. Contrary to expectation, we observed dynamic growth followed by release of cells. This unstable local dynamics could lead to a dispersal of cells, which may enable the total regional population downstream to persist as reported in literature.⁴⁹ Additional investigations with varying microstructures and flow geometries should improve the understanding of biofilm cycles and their importance in downstream infection due to releases of bacterial cells.

CONCLUSIONS

We have shown that by coupling synchrotron-radiation-based Fourier transform infrared (SR-FTIR) spectromicroscopy with a simple open-channel thin-film microfluidic system, one can monitor directly bacteria activity and its biochemistry at a molecular level within a biofilm over a long time. Our results demonstrate a multiple-molecule sensitivity with a micrometer spatial resolution. We envision that this real-time and label-free chemical imaging ability can be advanced further by coupling with more sophisticated microfluidic devices.^{50–53} This might then be used to investigate many important microbial systems, including harmful processes, such as chronic bacterial infections, or beneficial processes, such as energy production in microbial fuel cells. We

- (49) Hassell, M. P.; Comins, H. N.; May, R. M. *Nature* **1994**, *370*, 290–292.
- (50) Davidsson, R.; Boketoft, A.; Bristulf, J.; Kotarsky, K.; Olde, B.; Owman, C.; Bengtsson, M.; Laurell, T.; Emneus, J. *Anal. Chem.* **2004**, *76*, 4715–4720.
- (51) Gomez-Sjoberg, R.; Leyrat, A. A.; Pirone, D. M.; Chen, C. S.; Quake, S. R. *Anal. Chem.* **2007**, *79*, 8557–8563.
- (52) Koo, O. K.; Liu, Y. S.; Shuaib, S.; Bhattacharya, S.; Ladisch, M. R.; Bashir, R.; Bhunia, A. K. *Anal. Chem.* **2009**, *81*, 3094–3101.
- (53) Lam, R. H. W.; Kim, M. C.; Thorsen, T. *Anal. Chem.*, in press.

also envision combining our approach with emerging imaging concepts such as the guided confocal microscope⁵⁴ to enable detailed mechanistic studies of cell–biofilm interactions and their relationship to gene expressions at the single-cell level. If we can simultaneously study via fluorescence a cell's gene expression and the cell's interactions with the biofilm matrix, we will be able to link specific gene expression patterns/cascades to initiation of the biofilm as well as release of planktonic cells.

ACKNOWLEDGMENT

This work was supported by the U.S. Department of Energy Office of Biological and Environmental Research's Structural Biology Program through Contracts DE-AC02-05CH11231 and

KP1501021 with Lawrence Berkeley National Laboratory. Thanks to Dr. Tina Van Dyk of E. I. du Pont de Nemours and Co. for providing *Escherichia coli* DPD2794.

SUPPORTING INFORMATION AVAILABLE

Text describing flow field visualization and simulation, microfluidic SR-FTIR efficacy verification, fluorescence microscopy and measurements, and bioluminescence MMC sublethal toxicity assay, figures showing various results of SR-FTIR study, and reference list. This material is available free of charge via the Internet at <http://pubs.acs.org>

Received for review July 10, 2009. Accepted September 7, 2009.

AC9015424

(54) Cang, H.; Xu, C. S.; Montiel, D.; Yang, H. *Opt. Lett.* **2007**, *32*, 2729–2731.